Lawrence Berkeley National Laboratory

LBL Publications

Title

4D-STEM of Beam-Sensitive Materials

Permalink

https://escholarship.org/uc/item/4x44d9j0

Journal

Accounts of Chemical Research, 54(11)

ISSN

0001-4842

Authors

Bustillo, Karen C

Zeltmann, Steven E

Chen, Min

et al.

Publication Date

2021-06-01

DOI

10.1021/acs.accounts.1c00073

Peer reviewed

eScholarship.org Powered by the California Digital Library
University of California

4D-STEM of Beam-sensitive Materials

Karen C. Bustillo[1], Steven E. Zeltmann[2], Min Chen[2], Jennifer Donohue[2], Jim Ciston[1], Colin Ophus[1], Andrew Minor[1,2]*

[1]National Center for Electron Microscopy, Molecular Foundry, Lawrence Berkeley National Laboratory, Berkeley, CA 94720

[2]Department of Materials Science and Engineering, University of California, Berkeley, CA 94720

CONSPECTUS

Scanning electron nanobeam diffraction, or 4D-STEM (four-dimensional scanning transmission electron microscopy), is a flexible and powerful approach to elucidate structure from "soft" materials that are challenging to image in the transmission electron microscope because their structure is easily damaged by the electron beam. In a 4D-STEM experiment, a converged electron beam is scanned across the sample and a pixelated camera records a diffraction pattern at each scan position. This four-dimensional dataset can be mined for various analyses, producing maps of local crystal orientation, structural distortions, crystallinity, or different structural classes. Holding the sample at cryogenic temperatures minimizes diffusion of radicals and the resulting damage and disorder caused by the electron beam. The total fluence of incident electrons can easily be controlled during 4D-STEM experiments by careful use of the beam blanker, steering of the

localized electron dose, and by minimizing the fluence in the convergent beam thus minimizing beam damage. This technique can be applied to both organic and inorganic materials that are known to be beam-sensitive; they can be highly crystalline, semi-crystalline, mixed phase, or amorphous (examples are shown in Figure 1). One common example is the case for many organic materials that have a π-π stacking of polymer chains or rings on the order of 3.4-4.2 Å separation. If these chains or rings are aligned in some regions, they will produce distinct diffraction spots (as would other crystalline spacings in this range), though they may be weak or diffuse for disordered or weakly-scattering materials. We can reconstruct the orientation of the π-π stacking, the degree of π-π stacking in the sample, and the domain size of the aligned regions. This account summarizes illumination conditions and experimental parameters for 4D-STEM experiments with the goal of producing images of structural features for materials that are beam-sensitive. We will discuss experimental parameters including sample cooling, probe size and shape, fluence, and cameras. 4D-STEM has been applied to a variety of materials, not only as an advanced technique for model systems, but as a technique for the beginning microscopist to answer materials science questions. It is noteworthy that the experimental data acquisition does not require an aberration-corrected TEM, but can be produced on a variety of instruments with the right attention to experimental parameters.

KEY REFERENCES

- Panova, O.; Ophus, C.; Takacs, C. J.; Bustillo, K. C.; Balhorn, L.; Salleo, A.; Balsara, N.; Minor, A. M., Diffraction imaging of nanocrystalline structures in organic semiconductor molecular thin films. *Nature Materials* **2019,** *18*, 860-866.[1] Using 4D-STEM, the orientation of π-π stacking from two different molecular film systems was

visualized as flow-lines providing an orientation map that shows overlapping grains. The resulting structure maps show grains with sharp grain boundaries and overlapping grains, as well as liquid-crystal like structures that contain disclinations representing singularities in the director field.

- Gallagher-Jones, M.; Bustillo, K. C.; Ophus, C.; Richards, L. S.; Ciston, J.; Lee, S.; Minor, A. M.; Rodriguez, J. A., Atomic structures determined from digitally defined nanocrystalline regions. *Iucrj* **2020,** *7*, 490-499.[2] The atomic structure of this protein crystallite was confirmed with high spatial resolution using a 4D-STEM tomography series, a 4D-STEM dataset acquired at each 1° tilt step in a ±30° tilt range. The 4D-STEM technique was compared to similar results from MicroED and selected area diffraction.
- Panova, O.; Chen, X. C.; Bustillo, K. C.; Ophus, C.; Bhatt, M. P.; Balsara, N.; Minor, A. M., Orientation mapping of semicrystalline polymers using scanning electron nanobeam diffraction. *Micron* **2016,** *88*, 30-36.[3] 4D-STEM was applied to a photovoltaic polymer blend to map the size and orientation of crystallites, as well as the degree of crystallinity.

Introduction

As a technique, scanning electron nanobeam diffraction, or 4D-STEM,[4] can be applied to electron beam-sensitive materials to produce structural maps from a series of diffraction patterns acquired during a scanning transmission electron microscopy (STEM) image. Cooling the sample with LN_2 to slow diffusion of ionizing species,[5] in combination with 4D-STEM acquisition, allows one to collect data from some of the most electron beam-sensitive materials. Samples can be

transferred into the TEM in the frozen vitreous state allowing for imaging in a hydrated state as is commonly described with the term "Cryo-EM", or they can be transferred as dry samples at room temperature and then cooled only during electron beam irradiation. This report will focus on the latter, although 4D-STEM could be applied to vitreous samples.[6] For samples that are easily damaged by the electron beam, the luxury of finding the right location, doing careful focus, and perhaps spectroscopy as a function of position is seldom possible. Instead, making every incident electron count and keeping track of the numbers of electrons used is critical. Ultimately, the goal is to optimize the signal-to-noise ratio (SNR) in the raw data and enable dose control, both of which can be facilitated using 4D-STEM.

The kinds of material systems that are appropriate for cryogenic 4D-STEM include: organic materials such as polymers[3], small molecules[1], and proteins[7]; inorganic materials such as perovskites, oxides, 2D materials, organic-frameworks, or composite materials such as nanoparticle assemblies in contact with an organic component. Typical diffraction patterns showing the wide distribution of raw data types are shown in Figure 1a-f.

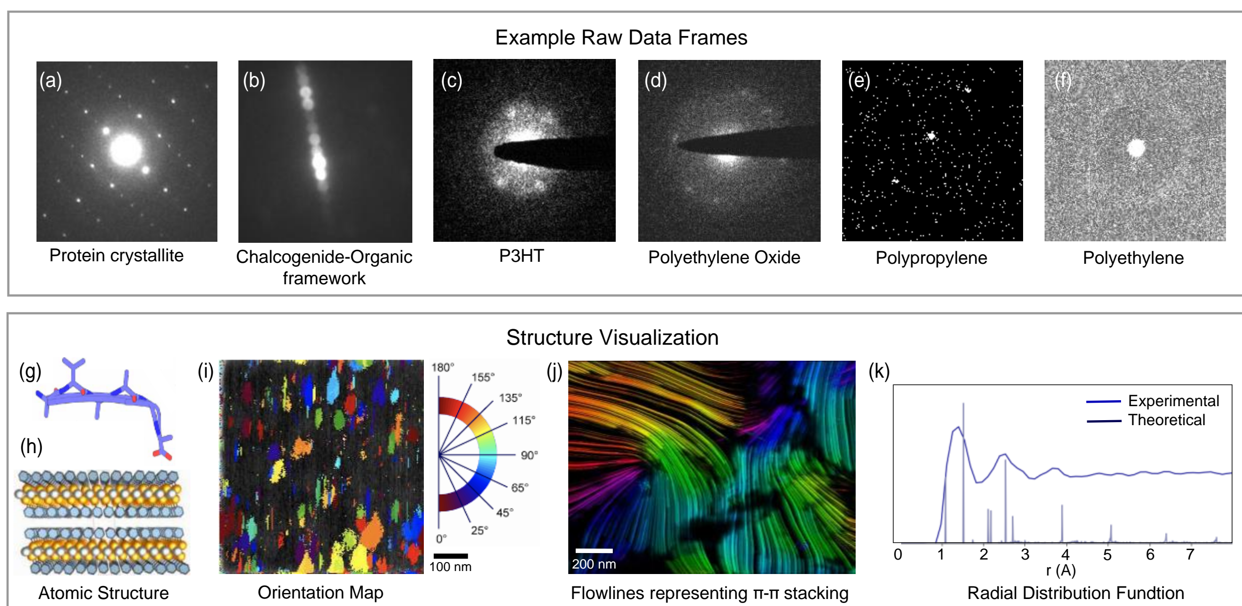

Figure 1. Example diffraction patterns and structure maps. a) Protein crystallite;[2] b) Ag-Se-organic layered material;[8] c-f) Semi-crystalline organic materials; g) Atomic structure of protein crystallite;[2] h) Layered structure of Ag-Se-organic framework;[8] i) Orientation map of π-π stacking in acid-polyethylene;[9] j) Flowlines representing overlapping grains from organic small molecule;[1] k) Radial distribution function from polyethylene. Figure 1a and 1g adapted with permission from ref. 2. Copyright 2020 International Union of Crystallography. Figure 1h reproduced with permission ref. 7. Copyright 2019 American Chemical Society.

In addition to being easily altered by the electron beam, many of the materials of interest are weakly scattering. They may be comprised of light elements that have a weak electrostatic potential, or the long-range order may be compromised, causing the signal to be spread in reciprocal space or to be mixed with signal from disordered regions. These kinds of materials often produce little image contrast or images that are difficult to interpret in a conventional bright-field or dark-field TEM image. In general, we seek structural information in the form of image contrast; Figure 1g-k shows several examples of maps of local structure and orientation.

The 4D-STEM technique uses a focused electron beam that scans across the TEM sample (Figure 2a). At each X and Y probe position, a 2D diffraction pattern is acquired with a pixelated camera. The two reciprocal space dimensions of the diffraction pattern, k_x and k_y, together with the real space probe positions of x and y are the four dimensions referred to in the term '4D-STEM'. A typical 4-dimensional dataset might contain 100 x 100 probe positions or 10,000 diffraction patterns.

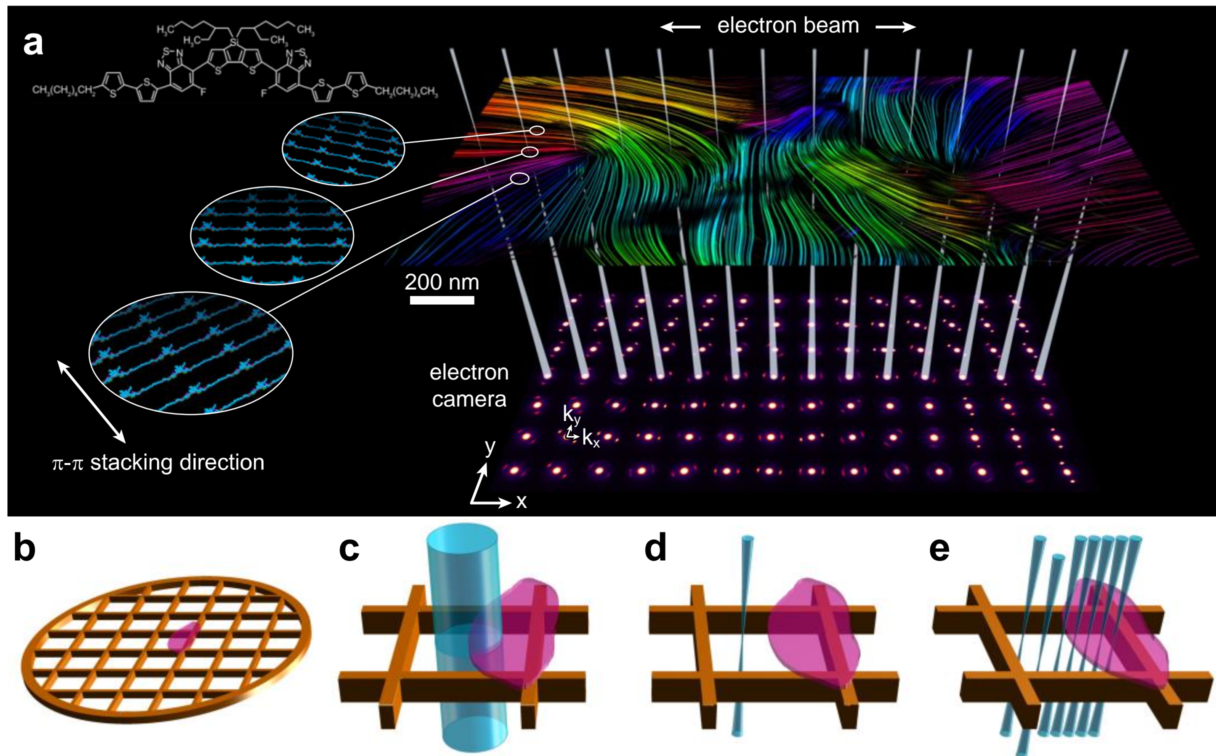

Figure 2. 4D-STEM experiment. a) Schematic of focused beam stepping across organic small molecule shown in upper left. The conjugated backbone is represented by colored lines. π-π stacking generates diffraction patterns; some frames show multiple pairs of reflections indicating overlapping grains and other frames contain only a weak amorphous halo indicating that region is either non-crystalline or does not have π-π stacking aligned in a diffracting condition; b) TEM sample grid with microtome slice; c) TEM parallel beam exposes large area of sample; d) Convergent beam limits area exposed; e) Once sample is found, probe is moved to unexposed sample for each new dataset.

The sensitivity of the sample to the electron beam varies greatly for different materials.[10,11] In the simplest observation, one experiences a decrease in the diffracted signal over time or perhaps no diffracted signal in the parallel TEM diffraction condition because the crystalline fraction is a

small part of the total. The critical dose, a fluence that causes the diffracted spots to decrease to $1/e$ in intensity, is reported for different materials (see recent review by Egerton).[10] The beam sensitivity depends not only on the material, but also on the synthesis and morphology. As a practical example, we have observed solution phase crystallites of polyethylene with order that lasts seconds at room temperature, while the order in a less-crystalline polyethylene phase is undetectable without cooling and a low-noise counting detector. Many samples are damaged with a few pA probe current and 50 ms dwell time (time at each scan position) to the point of forming a hole; others can be scanned multiple times allowing for a tomographic series of 4D-STEM datasets.[2] In addition to damage due to radiolysis, it is possible that electrostatic charging effects enhance the damage.[10,12] With the exception of graphene, we have found no advantage to performing 4D-STEM at accelerating voltages lower than 300kV; radiolysis is the presumed damage mechanism and this type of damage increases with decreasing accelerating voltage.[13]

One advantage of using STEM instead of parallel beam TEM is the spatially-resolved control of dose that can be a more straightforward approach for limiting exposure, especially for the non-expert microscopist. As shown in Figure 2c, conventional TEM exposes an area of the sample that is 100 nm to a few microns, and there is a habit of spreading and condensing the beam as the magnification is changed without paying attention to the size of the illuminated area and the position of the stage. In contrast, a STEM image only illuminates the square area scanned (Figure 2d), and the scan position is saved in the image tags. By unblanking the beam only when acquiring an image, the regions nearby will remain unexposed (Figure 2e). In many cases it is necessary to work 'without seeing', meaning the beam is blanked while moving around the sample and unblanked only when acquiring a dataset. Working 'without seeing' in this manner means that there is no opportunity to focus the sample. In conventional TEM, focusing takes time and

electron dose and while it can be performed adjacent to the region of interest, parallel beam imaging is not as robust to defocus as acquiring diffraction patterns. Working 'without seeing' also means that there should be large areas of sample on every grid so that time is not wasted looking for the sample. In practice, it is sometimes possible to acquire a low-magnification (~140X) STEM image quickly at the beginning of the session to confirm the location of the region of interest. Microtomed sections can often be seen and photographed in the optical microscope, in order to orient the section with respect to the center of the grid. Acquiring movies of the diffraction while moving the sample quickly while scanning can also help locate the signal. Constant use of the pre-specimen beam blanker is essential. The first goal in any attempt to image these materials is to acquire some detectible signal in reciprocal space; this is usually detected by the eye as the frames flash on the computer monitor. In many cases, cooling the sample makes the difference between capturing some signal or none at all, and the final optimization of parameters can be done empirically.

Sample Preparation and cooling

Typically, samples are supported on a TEM grid with an amorphous support that is several to 20 nm thick. The "lacey" structures in some TEM grids provide features on which to focus, as well as to track sample drift. The samples can be spin-cast resulting in a thin film, drop-cast from a solution, thinned with a focused ion beam, or embedded in a resin and then sliced with a microtome knife, often at cryogenic temperatures, to produce thin sections. 4D-STEM does not require ultra-thin sections; <200 nm thick samples are acceptable at 300kV accelerating voltage for weakly scattering samples. However, if the thickness of the sample starts to include many domains through the thickness, the diffraction patterns can be challenging to analyze.

The sample is placed in a TEM holder and the foot-long copper rod that holds the sample is cooled by an external liquid nitrogen dewar after the sample holder is inserted into the TEM (Figure 3a). The sample is cooled, usually to the lowest temperature possible, although one can control the temperature with a local heater over the range of -10°C to -170°C. Because the cooling of the copper rod causes contraction/expansion, the sample drifts severely during the first ~60 minutes of cooling. Eventually the sample drift slows to ~0.5 nm/s, but its direction is predictably along the holder axis. It is necessary to take into account the number of pixels in the fast scan direction, the dwell time, step size and drift rate in order to prevent sampling the same region twice. If the magnitude and direction of the drift is known, one can place the fast scan direction perpendicular to the holder axis and scan opposite to the drift, and consequently the reconstructed map shows more of a stretch and less of a skew.

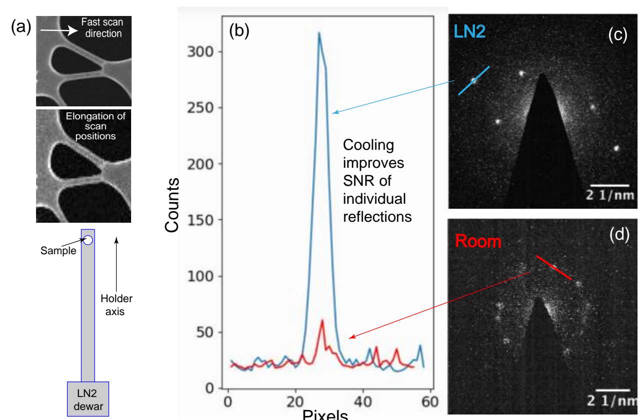

Figure 3. Cryogenic 4D-STEM. a) Drift along holder axis causes the reconstructed image to be stretched compared with the actual region; b) Line scan from acid-polyethylene sample[9, 14] shows advantage in SNR when cooling; c) LN_2; (d) 20°C. The best diffraction frame from each dataset was chosen to make the comparison. Image 3c,d adapted with permission ref. 14. Copyright 2020 Cambridge University Press.

Figure 3b highlights the SNR improvement when keeping the sample cold. Here we compare a line scan through the strongest reflections from datasets acquired near -170°C (Figure 3c) and 20°C (Figure 3d). The improvement is material dependent, but we observe a factor of ~2-6 improvement in SNR at the lower temperatures with others reporting similar numbers.[10]

Probe size and shape

The semi-convergence angle, α, is defined by the probe forming aperture (usually just below the second condenser lens, C2) and the angle of the beam when it hits the aperture (Figure 4a). One can tailor the angle by using different sized apertures and, in a 3-condenser TEM, by adjusting the relative strength of the second and third condenser lenses. The semi-convergence angle has an inverse effect on the size of the probe - the larger the α, the smaller the probe. Typical semi-convergence angles for beam-sensitive materials that require cryogenic conditions are 0.5 – 0.01 mrad, in contrast to HRSTEM which uses α = 10-30 mrad, or 4D-STEM strain mapping, which uses α = 1-4 mrad. In reciprocal space, the size of the Bragg disks in the diffraction patterns are proportional to α. For many 4D-STEM applications one wants to separate the reflections, so that they can be individually located by template matching. For beam-sensitive semi-crystalline materials, it is advantageous to make the reflections even smaller or sharper.[14] Reducing the convergence angle while maintaining the same probe current localizes the signal into fewer pixels on the detector, helping to boost the signal above the noise floor of the detector as shown in Figure 4b. The $<$0.5 mrad beam is quite parallel with its cross-over point suitably aligned for positional control by the scanning deflectors.

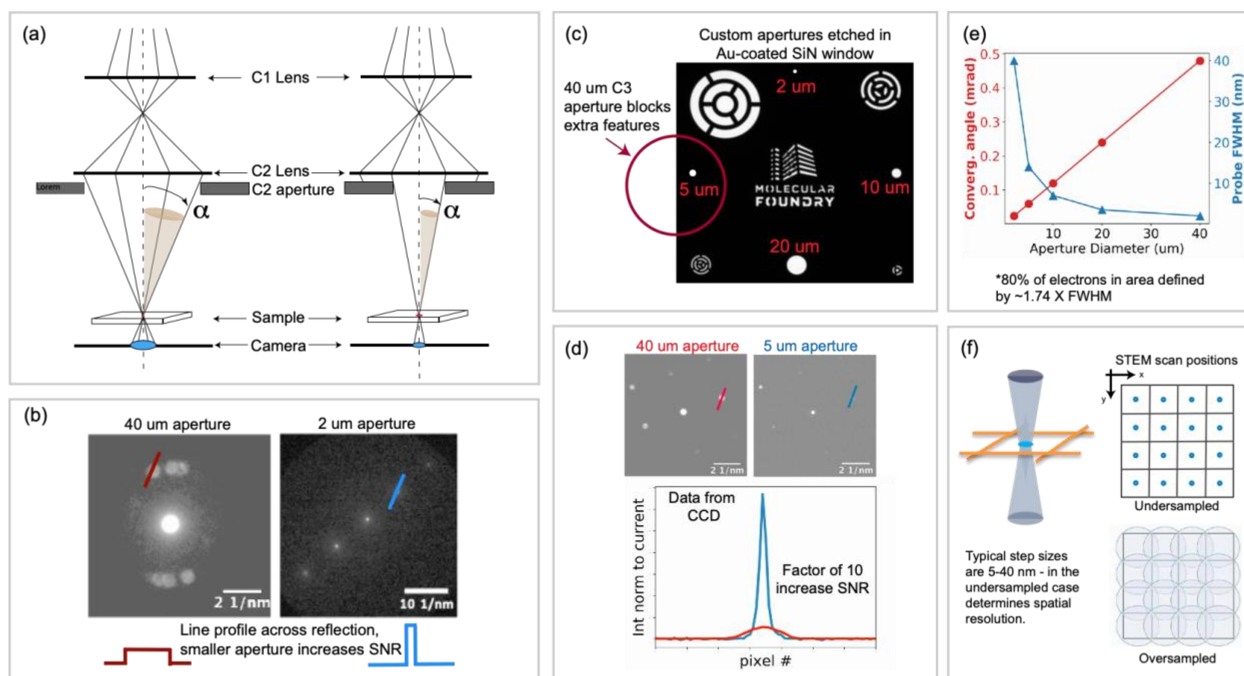

Figure 4. Small probe forming apertures. a) Ray diagrams for two different aperture sizes showing semi-convergence angle (α), and corresponding size of diffraction spots; b) Squeezing electrons into fewer pixels on the camera increases SNR, comparison of 40µm aperture (organic small molecule) and 2µm aperture (rubrene); c) Custom apertures on Au-coated SiN window, red circle is additional aperture that selects the 5µm;[15] d) Experimental comparison of two apertures; Au foil measured on CCD shows 10X improvement in SNR with smaller aperture for the same fluence; e) Real-space probe size (blue) is inversely proportional to α (red); f) Probe intersecting sample determines exposure area, typical step sizes of 5-40 nm can result in either undersampled or oversampled region of interest. Image 4b reproduced with permission ref. 14. Copyright 2020 Cambridge University Press.

A typical probe forming aperture is 40 to 150µm in diameter, but condenser apertures exist that are 20, 10, 5 or 2µm in diameter.[15,16] The aperture plate shown in Figure 4c has 8 different

apertures; the bullseye design helps with strain mapping precision.[16, 17] The 3mm aperture plate fits in many TEM aperture rods; it requires an aperture 40-70µm downstream (usually below C3) to select the aperture of interest. These smaller apertures allow for control of the convergence angle to smaller angles than is typical. The small apertures have the added advantage that they can reduce the fluence of electrons, which is especially helpful for TEMs that do not have a monochromator with continuously adjustable gun lens to control the fluence. Data from an oriented Au foil showing the measured difference of SNR between 40µm and 5µm apertures is shown in Figure 4d. For a given electron fluence, the smaller aperture realizes a factor of 10 improvement in SNR. Theoretically, the peak height should depend on the square of the aperture diameter,[18] but because these images were acquired on a scintillator-coupled camera, the point spread function causes "blooming" over neighboring pixels and only a factor ~10 is realized. What is most significant for the beam-sensitive materials, is that one can reduce the electron fluence by a factor of 10 without compromising SNR by using a smaller aperture.

The disadvantage of using a smaller aperture and corresponding small convergence angle is that it increases the size of the probe in real space. The plot in Figure 4e shows how the FWHM of the probe, measured in real-space on the camera, increases with decreasing aperture diameter. Similar numbers have been reported by those who perform fluctuation microscopy and intentionally want a few-nm-sized probe.[18] Because the probe-forming aperture is sharp in Fourier space, the shape of a STEM probe in real space is an Airy disk pattern, which in its most focused state can be approximated by a Gaussian, although the true Airy disk does possess tails.[19] The probe size for a 0.5 to 0.01 mrad semi-convergence angle has a FWHM of typically 1-15 nm. In actuality this FWHM represents only ~50% of the electron fluence; ~80% of the fluence is contained in 1.74 x FWHM, with long tails that extend nanometers from its center. However, measurement of the

FWHM from a real-space image of the probe is easy to make as a check of the illumination conditions. Depending on the step size of the scan, the size of the probe in real space can limit the spatial resolution of the final structure map.

A critical experimental parameter for 4DSTEM experiments is the step size, or the distance between probe positions. For many beam-sensitive materials that lose their order from damage due to radiolysis, there is a damage ring (sometimes called "collateral damage") that extends well beyond the first minimum of the airy disk.[10, 20] This damage ring then defines the closest one can separate the probe positions without illuminating a damaged region that provides less or no useful signal. Often this step size is what defines the spatial resolution in real space; the scan positions are commonly spaced 10-40 nm apart, often significantly larger than the probe size. Two extremes of sampling are shown in Figure 4f. In one case the material is oversampled with a step size that is smaller than the area illuminated by the probe and in this case the area of the probe is what defines the spatial resolution. In the other extreme, the material is undersampled to avoid the damage ring or perhaps to cover a large region of interest, and in this case the spatial resolution is defined by the step size.[10] During the experiment the loss of diffraction information is a clear indicator that the damage radius exceeds the step size: the first scan position will have signal and subsequent scan positions will produce no signal.

In real space the sample is "in focus" when it is placed at the cross-over point of the beam, (Figure 5a-b). If the sample is out of focus and not at this cross-over point (Figure 5c), then the intersection area is larger as shown in Figure 5a. If the beam is strongly defocused, then the shape of the airy rings become more dominant, and the tails start to contain more of the electrons as shown in Figure 5d. Therefore, another advantage of using a smaller semi-convergence angle is that it increases the depth of focus. This means that the sample does not need to be at the perfect

crossover point, and yet it will be close enough to not significantly increase the intersected area of the probe with the sample, nor change the sharpness of the reflections. A large depth of focus means that it is hard to focus in STEM mode, but one can get around this by temporarily inserting a large aperture without changing the C2/C3 conditions, finding the eucentric height of the sample and then going back to the smaller aperture. For the example of a 0.12 mrad semi-convergence angle the sample needs to have a z-height which is +/- 30μm in order to be "in focus"; in this measurement, "in focus" was defined by a change in maximum intensity of the center peak by <15%. This allows the sample to change height and bend across the grid and not compromise the imaging conditions.

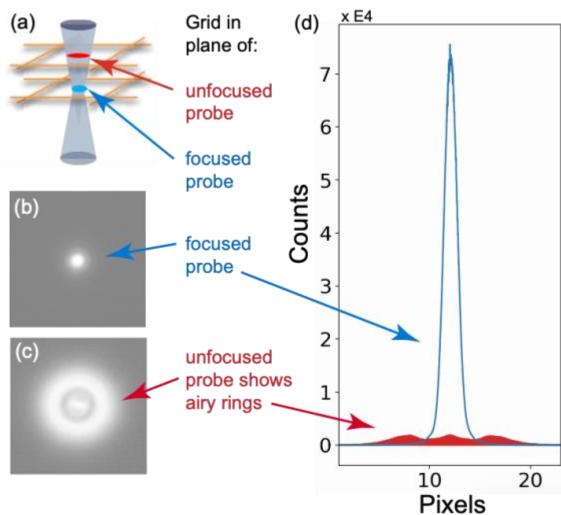

Figure 5 Probe shape a) Focus of STEM image defined by placing sample at cross-over height, sample not in this plane intersects the probe in a defocused state; b) Real-space image of focused probe; c) Real-space image of defocused probe; d) Line scan through focused (blue) and defocused (red).

In analogy to refractive lenses, we consider the probe-forming aperture as the numerical aperture (NA) of the illumination system. Table I lists how parameters of interest should depend on the

NA.[18, 21] Row A lists semi-convergence angle as indicated in the TEM software. Row B shows improvement in peak height of the signal from a CCD camera for a given electron fluence; this value is less than theoretically expected as the point spread function limits accurate measurement on the CCD. Row C is measured screen current, which scales appropriately with the indicated semi-convergence angle. Row D is the real-space FWHM measured at high magnification. Row E is estimated depth of focus.[21]

	I Dependence on Numerical Aperture (NA)	II Measured with 40μm Aperture	III Measured with 5μm Aperture
Semi-convergence angle	NA	0.48 mrad ind.	60 μrad ind.
SNR or peak height	$1/(NA)^2$	1	10
Beam Current	$(NA)^2$	6 pA	94 fA
Real space FWHM	1/(NA)	2 nm	14 nm
Depth of focus (theoretical)	$1/(NA)^2$	~10μm	>>10μm

Table 1 Probe parameters as a function of probe-forming aperture or numerical aperture, NA.

Because of the need for small convergence angles, the 3-condenser TEMs are set in "Microprobe" STEM mode; the mini-condenser lens is active with a large angle range. There is no advantage to using a probe-corrected TEM for these experiments as the probe size is limited by diffraction from the probe-forming aperture, rather than by aberrations in the lenses.[18]

Electron Fluence

The fluence, or dose, in $eÅ^{-2}$ describes the total sum of electrons incident in a region of the sample. To calculate the fluence, the following steps are used: (1) measure the screen current on the calibrated fluorescent screen in pA, (2) convert to electrons (1pA = $6.24x10^6$ e/s), (3) multiply by the exposure time, and (4) divide by the relevant area. Sometimes the flux, or dose rate, in $eÅ^{-}$

$^{2}s^{-1}$ is important.[22] However, for many materials it is believed that the damage is independent of dose-rate and instead is dependent on total dose.[10] In STEM imaging where oversampling is typical, the relevant area is the scanned area and the exposure time is the frame time; this is appropriate in 4D-STEM in cases where we are not undersampling. However, in the example of Figure 4f where the material is undersampled, such a measurement would under-report the fluence from the area that generates the signal. Instead, we take the relevant area to be the area defined by the FWHM as an easy measurement with the time being the dwell time. Experiments with beam-sensitive materials can range from 0.5–10,000 eÅ^{-2}. Table 2 shows comparisons of fluence for different conditions. A common benchmark for low dose imaging is a fluence <20 eÅ^{-2}.[23] As can be seen by the boxes highlighted in yellow in Table 2, reducing the fluence by using a small aperture can achieve these low-dose conditions; the spatial resolution of the structure map is now limited by the large size of the real-space probe. The point to recognize is that the signal arises from the area that is illuminated, and it is that area that should be used to calculate the fluence. The small beam current is measured on the fluorescent screen at a weak C1 excitation (small spot#) and then extrapolated to the spot size used. A dwell time of 2-50 ms is typical, but this parameter can also be used to tune the fluence.

	40µm Aperture	5µm Aperture
Beam Current	6 pA	94 fA
Real Space FWHM	2 nm	14 nm
Step size	10 nm	10 nm
Dwell time	50 ms	50 ms
Fluence 1µm x 1µm image	200 eÅ^{-2}	~3 eÅ^{-2}
Fluence using FWHM	6000 eÅ^{-2}	~2 eÅ^{-2}

Table 2 Fluence (eÅ^{-2}) measured two ways: the total image area and probe area.

Detectors

During a 4D-STEM experiment a pixelated camera is used to acquire diffraction patterns. Either a scintillator-transduced (CCD or CMOS) or a direct-electron (hybrid pixel array detector or monolithic active pixel, counted or integrated) camera[24] can be used, although the subtleties of their operation and performance will dictate the experiment. Acquiring diffraction patterns from a beam-sensitive material usually does not require high reciprocal-space sampling, so 512 x 512 pixels is often enough. There is a need for dynamic range because the unscattered beam can be strong compared to the scattered beam, and the reflections can be of variable intensity as the probe scans over regions of varying crystallinity, although if one is not using the intensity of the disks in the analysis, it is acceptable to saturate some reflections intentionally. Because there exists sample drift (especially when cooling), the frame rate (frames per second, fps) is important. The figure of merit that addresses both sensitivity and noise of the sensor is the detector quantum efficiency (DQE);[25] the DQE is important because of the need to maximize the SNR of the diffracted spots. For most applications, a CCD running at 20 fps is a good compromise of speed and dynamic range.

The big advantages to using a direct electron camera for beam-sensitive materials are higher DQE and faster frame rate.[26, 27] The camera frame rate dictates the speed of data acquisition: at 20 fps (dwell time = exposure time = 50ms), a 100x100 position scan will take 8 minutes; at 400 fps it will take 25 sec. In addition to the sensor having a higher DQE, many direct electron cameras can be operated in "counting mode", resulting in lower noise. In order to operate in counting mode, a pixel fill factor of ~1% is recommended such that the probability of acquiring >1 electron per pixel is low.[24] The relevant pixel fill factor is for the regions within the reflections. Such a low

fill factor is achieved by a combination of reducing the flux of electrons as well as a fast frame rate. Because each frame has little data, many frames need to be summed. Consequently, although the camera has a high frame rate, the number of summed frames may approach the same 50 msec exposure that is common on a CCD camera, and so the number of pixels in the STEM scan is still limited by the speed. Newer direct electron cameras, like the 4D camera at NCEM[28, 29] running at 87,000 fps, make higher fluxes possible while maintaining a ~1% fill factor.

Because many of the soft materials are weakly scattering, the unscattered beam is much stronger than the reflections of interest. Consequently, the unscattered beam must either be blocked by a beam stop or the camera must be robust enough to withstand a large flux of electrons in the central spot. The shape and size of the beamstop may limit the camera length, and it certainly adds to the trouble of aligning all the diffraction patterns in post-processing. With large area (>100 nm) scans, there can be sway in the beam due to misaligned descan, which can move the beam out from under the beam stop. An active pixel direct electron camera can be damaged by a direct beam and so these cameras usually retract automatically when a dangerous level is reached limiting the dynamic range. The hybrid pixel array direct electron cameras, like the EMPAD[30] or Medipix,[26] were designed as high dynamic range cameras that are able to withstand the full flux of the unscattered electron beam.

Some pixelated cameras are placed at the end of an energy filter – a prism that spreads the electrons in energy allowing for a slit to be placed such that the diffraction image is constructed of electrons that have lost only a certain amount of energy. We have used this feature to bracket the zero-loss peak with a 15 eV slit, which removes some electrons that are inelastically scattered to improve SNR of the diffraction spots; this is especially useful for thick samples. While the pixelated camera is acquiring the diffraction patterns, it is common, although not necessary, to

acquire a conventional STEM image, albeit pixelated, with a monolithic annular dark field detector.[27] A similar STEM image could be reconstructed from the 4D-dataset.

Data Analysis

Once a dataset of ~10,000 frames is acquired, computer algorithms process the data to reconstruct a real-space map.[31, 32] One could imagine choosing one reflection (a disk of pixels, k_x-k_y, in reciprocal space) and reconstructing a real-space image of 100x100 pixels where the pixel intensity is the strength of that reflection.[31] This real-space reconstruction is analogous to a conventional dark-field image obtained by placing an objective aperture in the TEM around a diffracted spot and acquiring a dark-field TEM image. The advantage of 4D-STEM is that one can construct unlimited virtual apertures or combinations of apertures to explore contrast mechanisms, all in post-processing. Similarly, one can sum diffraction signals from an arbitrary collection of scan spots and then display the resulting diffraction pattern, analogous to selected area diffraction in conventional TEM. Thus, nanobeam diffraction, enables low-dose determination of crystal orientation over large, real-space features. This feature of 4D-STEM has been applied to beam-sensitive battery materials,[33] catalytic nanoparticles,[34] and framework materials, and it has potential to identify orientation in perovskite[35] and oxide materials that are often beam-sensitive.

Several open-source packages have been developed to analyze datasets,[27, 36] such as py4DSTEM[32] and pyXem.[37] First steps in the analysis include: aligning all diffraction frames, subtracting a background, and correcting for ellipticity introduced by stigmation in objective or projector lenses. Then, a cross-correlation is performed against a template of the probe-forming aperture to identify the positions of Bragg reflections. If the material exhibits short- or medium-

range order, a radial distribution function (rdf) can be generated that tracks correlations which correspond to bonding arrangements. If distinct rdf fingerprints exist, one can create a phase map distinguishing the different regions.[38] Even for semicrystalline, mixed phase or amorphous samples, measurements using 4D-STEM can allow for comparison of different synthesis methods or processing conditions.[1]

Conclusion

4D-STEM is an emerging technique that can visualize structural contrast in materials that are conventionally challenging to image. In this account we have discussed experimental parameters that make it possible for even a beginning microscopist to take advantage of this rich technique. In the future, the technique will be improved by faster cameras and more comprehensive data analysis pipelines.

BIOGRAPHIES

Karen C. Bustillo is a staff member at the National Center for Electron Microscopy, Molecular Foundry, Lawrence Berkeley National Laboratory.

Steven E. Zeltmann is a PhD candidate in the Department of Materials Science and Engineering at the University of California, Berkeley.

Min Chen is a graduate student in the Department of Materials Science and Engineering at the University of California, Berkeley.

Jennifer Donohue is a PhD candidate in the Department of Materials Science and Engineering at the University of California, Berkeley.

Jim Ciston is a staff member at the National Center for Electron Microscopy Facility, Molecular Foundry, Lawrence Berkeley National Laboratory.

Colin Ophus is a staff scientist working at the National Center for Electron Microscopy, Molecular Foundry, Lawrence Berkeley National Laboratory.

Andrew M. Minor is a Professor of Materials Science and Engineering at the University of California, Berkeley and the Facility Director at the National Center for Electron Microscopy, Molecular Foundry, Lawrence Berkeley National Laboratory.

ACKNOWLEDGMENTS

AM and MC were supported through the Electron Microscopy of Soft Matter Program, Office of Science, Office of Basic Energy Sciences, Materials Sciences and Engineering Division of the U.S. Department of Energy (DOE) under Contract No. DE-AC02-05CH11231. SEZ was supported by STROBE, an NSF Science and Technology Center, under Grant No. DMR 1548924. JD was supported by the Dow University Partnership Initiative Program. Work at the Molecular Foundry was supported by the Office of Science, Office of Basic Energy Sciences, of the U.S. DOE under Contract No. DE-AC02-05CH11231. JC acknowledges support from the Presidential Early Career Award for Scientists and Engineers (PECASE) through the US DOE. CO acknowledges support from the US DOE early career research award program. We thank Jenna Tan and Naomi Ginsberg for the rubrene sample. We would also like to thank other collaborators over the years including Karen Winey, Ouliana Panova, Nitash Balsara, Marcus Gallagher-Jones, Jose Rodriguez, Chris Takacs, Alberto Salleo, Luke Balhorn, Chelsea Chen, Xi Jiang, Brooke Kuei, Enrique Gomez, James Hohman, Alex Mueller and Christoph Gammer.

REFERENCES

1. Panova, O.; Ophus, C.; Takacs, C. J.; Bustillo, K. C.; Balhorn, L.; Salleo, A.; Balsara, N.; Minor, A. M., Diffraction imaging of nanocrystalline structures in organic semiconductor molecular thin films. *Nature Materials* **2019,** *18*, 860-866.

2. Gallagher-Jones, M.; Bustillo, K. C.; Ophus, C.; Richards, L. S.; Ciston, J.; Lee, S.; Minor, A. M.; Rodriguez, J. A., Atomic structures determined from digitally defined nanocrystalline regions. *Iucrj* **2020,** *7*, 490-499.

3. Panova, O.; Chen, X. C.; Bustillo, K. C.; Ophus, C.; Bhatt, M. P.; Balsara, N.; Minor, A. M., Orientation mapping of semicrystalline polymers using scanning electron nanobeam diffraction. *Micron* **2016,** *88*, 30-36.

4. Ophus, C., Four-Dimensional Scanning Transmission Electron Microscopy (4D-STEM): From Scanning Nanodiffraction to Ptychography and Beyond. *Microscopy and Microanalysis* **2019,** *25*, 563-582.

5. Grubb, D. T., Review of Radiation-Damage and Electron-Microscopy of Organic Polymers. *Journal of Materials Science* **1974,** *9*, 1715-1736.

6. Zhou, L. Q.; Song, J. D.; Kim, J. S.; Pei, X. D.; Huang, C.; Boyce, M.; Mendonca, L.; Clare, D.; Siebert, A.; Allen, C. S.; Liberti, E.; Stuart, D.; Pan, X. Q.; Nellist, P. D.; Zhang, P. J.; Kirkland, A. I.; Wang, P., Low-dose phase retrieval of biological specimens using cryo-electron ptychography. *Nature Communications* **2020,** *11*, 2773.

7. Gallagher-Jones, M.; Ophus, C.; Bustillo, K. C.; Boyer, D. R.; Panova, O.; Glynn, C.; Zee, C.-T.; Ciston, J.; Mancia, K. C.; Minor, A. M.; Rodriguez, J. A., Nanoscale mosaicity

revealed in peptide microcrystals by scanning electron nanodiffraction. *Communications Biology* **2019,** *2*, 26.

8. Schriber, E. A.; Popple, D. C.; Yeung, M.; Brady, M. A.; Corlett, S. A.; Hohman, J. N., Mithrene Is a Self-Assembling Robustly Blue Luminescent Metal-Organic Chalcogenolate Assembly for 2D Optoelectronic Applications. *Acs Applied Nano Materials* **2018,** *1*, 3498-3508.

9. Bustillo, K.; Panova, O.; Gammer, C.; Trigg, E.; Chen, X.; Yan, L.; Balsara, N. P.; Winey, K. I.; Minor, A., Development of Diffraction Scanning Techniques for Beam Sensitive Polymers. Microscopy and Microanalysis. **2016,** *22*, 492-493.

10. Egerton, R. F., Radiation damage to organic and inorganic specimens in the TEM. *Micron* **2019,** *119*, 72-87.

11. Russo, C. J.; Egerton, R. F., Damage in electron cryomicroscopy: Lessons from biology for materials science. MRS Bulletin **2019**, *44*, 935-941.

12. Jiang, N., Beam damage by the induced electric field in transmission electron microscopy. *Micron* **2016,** *83*, 79-92.

13. Egerton, R. F., Mechanisms of radiation damage in beam-sensitive specimens, for TEM accelerating voltages between 10 and 300 kV. *Microscopy Research and Technique* **2012,** *75*, 1550-1556.

14. Bustillo, K. C.; Zeltmann, S. E.; Chen, M.; Donohue, J.; Müller, A.; Ophus, C.; Ciston, J.; Minor, A. M., 4D-STEM of Beam-Sensitive Materials: Optimizing SNR and Improving Spatial Resolution. *Microscopy and Microanalysis* **2020,** *26,* 1734-1735.

15. Müller, A.; Durham, D.; Bustillo, K.; Allen, F.; Minor, A.; Ophus, C., Detailed Investigation of Silicon Nitride Phase Plates Prepared by Focused Ion Beam Milling. *Microscopy and Microanalysis* **2019,** *25(S2)*, 900-901.

16. Zeltmann, S. E.; Muller, A.; Bustillo, K. C.; Savitzky, B.; Hughes, L.; Minor, A. M.; Ophus, C., Patterned probes for high precision 4D-STEM bragg measurements. *Ultramicroscopy* **2020,** *209*, 112890.

17. Mahr, C.; Müller-Caspary, K.; Grieb, T.; Krause, F. F.; Schowalter, M.; Rosenauer, A., Accurate measurement of strain at interfaces in 4D-STEM: A comparison of various methods. *Ultramicroscopy* **2021,** *221*, 113196.

18. Bogle, S. N.; Nittala, L. N.; Twesten, R. D.; Voyles, P. M.; Abelson, J. R., Size analysis of nanoscale order in amorphous materials by variable-resolution fluctuation electron microscopy. *Ultramicroscopy* **2010,** *110*, 1273-1278.Voyles, P. M.; Bogle, S.; Abelson, J. R., Fluctuation Microscopy in the STEM. In *STEM, Imaging and Analysis*, Pennycook, S. J.; Nellist, P. D., Eds. Springer Science+Business Media, LLC: 2011; pp 725-756.

19. Voyles, P. M.; Bogle, S.; Abelson, J. R., Fluctuation Microscopy in the STEM. In *STEM, Imaging and Analysis*, Pennycook, S. J.; Nellist, P. D., Eds. Springer Science+Business Media, LLC: 2011; pp 725-756.

20. Egerton, R. F.; Lazar, S.; Libera, M., Delocalized radiation damage in polymers. *Micron* **2012,** *43*, 2-7.

21. Nellist, P. D., The Principles of STEM Imaging. In *Scanning Transmission Electron Microscopy*, Pennycook, S. J.; Nellist, P. D., Eds. Springer Science+Business Media, LLC: 2011; pp 91-115.

22. Jiang, N.; Spence, J. C. H., On the dose-rate threshold of beam damage in TEM. *Ultramicroscopy* **2012,** *113*, 77-82.

23. Baker, T. S.; Henderson, R., Electron cryomicroscopy. In *Crystallography of biological macromolecules, International Tables for Crystallography*, Rossmann, M. G.; Arnold, E., Eds. International Union of Crystallography 2006: Vol. F, pp 451-463.

24. McMullan, G.; Faruqi, A. R.; Clare, D.; Henderson, R., Comparison of optimal performance at 300 keV of three direct electron detectors for use in low dose electron microscopy. *Ultramicroscopy* **2014,** *147*, 156-163.

25. Faruqi, A. R.; McMullan, G., Electronic detectors for electron microscopy. *Quarterly Reviews of Biophysics* **2011,** *44*, 357-390.

26. Nord, M.; Webster, R. W. H.; Paton, K. A.; McVitie, S.; McGrouther, D.; MacLaren, I.; Paterson, G. W., Fast Pixelated Detectors in Scanning Transmission Electron Microscopy. Part I: Data Acquisition, Live Processing, and Storage. *Microscopy and Microanalysis* **2020,** *26*, 653-666.

27. MacLaren, I.; Macgregor, T. A.; Allen, C. S.; Kirkland, A. I., Detectors-The ongoing revolution in scanning transmission electron microscopy and why this important to material characterization. *Apl Materials* **2020,** *8*, 110901.

28. Ercius, P.; Johnson, I.; Brown, H.; Pelz, P.; Hsu, S.; Draney, B.; Fong, E.; Goldschmidt, A.; Joseph, J.; Lee, J.; Ciston, J.; Ophus, C.; Scott, M.; Selvarajan, A.; Paul, D.; Skinner, D.; Hanwell, M.; Harris, C.; Avery, P.; Stezelberger, T.; Tindall, C.; Ramesh, R.; Minor, A.; Denes, P., The 4D Camera – An 87 kHz Frame-rate Detector for Counted 4D-STEM Experiments. *Microscopy and Microanalysis* **2020,** *26*, 1896-1897.

29. Ciston, J.; Johnson, I.; Draney, B.; Ercius, P.; Fong, E.; Goldschmidt, A.; Joseph, J. M.; Lee, J. R.; Mueller, A.; Ophus, C.; Selvarajan, A.; Skinner, D. E.; Stezelberger, T.; Tindall, C. S.; Minor, A. M.; Denes, P., The 4D Camera: Very High Speed Electron Counting for 4D-STEM. *Microscopy and Microanalysis* **2019,** *25*, 1930-1931.

30. Tate, M. W.; Purohit, P.; Chamberlain, D.; Nguyen, K. X.; Hovden, R.; Chang, C. S.; Deb, P.; Turgut, E.; Heron, J. T.; Schlom, D. G.; Ralph, D. C.; Fuchs, G. D.; Shanks, K. S.; Philipp, H. T.; Muller, D. A.; Gruner, S. M., High Dynamic Range Pixel Array Detector for Scanning Transmission Electron Microscopy. *Microscopy and Microanalysis* **2016,** *22*, 237-249.

31. Gammer, C.; Burak Ozdol, V.; Liebscher, C. H.; Minor, A. M., Diffraction contrast imaging using virtual apertures. *Ultramicroscopy* **2015,** *155*, 1-10.

32. Savitzky, B.; Hughes, L.; Zeltmann, S.; Brown, H.; Zhao, S.; Pelz, P.; Barnard, E.; Donohue, J.; DaCosta, L.; Pekin, T.; Kennedy, E.; Janish, M.; Schneider, M.; Herring, P.; Gopal, C.; Anapolsky, A.; Ercius, P.; Scott, M.; Ciston, J.; Minor, A.; Ophus, C., py4DSTEM: a software package for multimodal analysis of four-dimensional scanning transmission electron microscopy datasets. *arXiv:2003.09523* **2020**.

33. Zeng, Z.; Zhang, X.; Bustillo, K.; Niu, K.; Gammer, C.; Xu, J.; Zheng, H., In Situ Study of Lithiation and Delithiation of MoS2 Nanosheets Using Electrochemical Liquid Cell Transmission Electron Microscopy. *Nano Letters* **2015,** *15*, 5214-5220.

34. Koshy, D. M.; Johnson, G. R.; Bustillo, K. C.; Bell, A. T., Scanning Nanobeam Diffraction and Energy Dispersive Spectroscopy Characterization of a Model Mn-Promoted Co/Al2O3 Nanosphere Catalyst for Fischer–Tropsch Synthesis. *ACS Catalysis* **2020,** *10*, 12071-12079.

35. Ran, J.; Dyck, O. O.; Wang, X.; Yang, B.; Geohegan, D. B.; Xiao, K., Electron-Beam-Related Studies of Halide Perovskites: Challenges and Opportunities. *Advanced Energy Materials* **2020,** *10*, 1903191.

36. Paterson, G. W.; Webster, R. W. H.; Ross, A.; Paton, K. A.; Macgregor, T. A.; McGrouther, D.; MacLaren, I.; Nord, M., Fast Pixelated Detectors in Scanning Transmission Electron Microscopy. Part II: Post-Acquisition Data Processing, Visualization, and Structural Characterization. *Microscopy and Microanalysis* **2020,** *26*, 944-963.

37. Johnstone, D. N.; Martineau, B.; Crout, P.; Midgley, P. A.; Eggeman, A. S., Density-based clustering of crystal (mis)orientations and the orix Python library. *Journal of Applied Crystallography* **2020,** *53*, 1293-1298.

38. Mu, X. K.; Mazilkin, A.; Sprau, C.; Colsmann, A.; Kubel, C., Mapping structure and morphology of amorphous organic thin films by 4D-STEM pair distribution function analysis. *Microscopy* **2019,** *68*, 301-309.

For Table of Contents Only